



Oxidation Behavior and Outward Diffusion of Al Along Oxide Grain Boundaries of FeCrAl Alloys Overdoped with Zr and Hf

Samer I. Daradkeh^{1,2,3} · Oscar Recalde⁴ · Marwan S. Mousa⁵ · Dinara Sobola^{3,6} · Torben Boll^{2,7}

Received: 18 July 2023 / Revised: 29 September 2023 / Accepted: 4 October 2023
© The Author(s) 2023

Abstract

The formation of the α -Al₂O₃ scale on reactive element (RE)-doped FeCrAl alloys is commonly believed to be primarily caused by inward oxygen transport along grain boundaries. However, this study suggests that metal ion outward diffusion also plays a role in the development of the oxide scales and their microstructural characteristics. The study examines the oxidation behavior and grain boundary outward diffusion of iron-chromium alloys containing ~10 at% aluminum and ~22 at% chromium, doped with an over-critical concentration of REs, i.e., Zr and Hf. All samples were investigated after thermal exposure at 1100 °C by scanning electron microscopy (SEM), transmission electron microscopy (TEM), and atom probe tomography (APT). As a result of the overdoping, a considerable increase in oxide growth, an increase in the depth of internal oxidation, and RE-oxide formation near and at oxide grain boundaries (GBs) were observed as a consequence of increased inward and outward diffusion. The effect of overdoping manifests itself differently depending on the RE type and amount due to different solubility, ionic size, and electronic structure of alumina. The sample with Zr retained the adhesion of alumina to the alloy after the first and second thermal exposure, while Hf overdoping resulted in severe spallation after the second thermal exposure.

Keywords Overdoping · Reactive element · Grain boundary · Alumina

Introduction

FeCrAl alloys are considered highly suitable for high-temperature applications such as heating elements and furnace linings due to their exceptional resistance to corrosion and oxidation [1–5]. They form an alumina scale (α -Al₂O₃) at 1100 °C, which is responsible for the excellent oxidation resistance. Alumina has excellent

Extended author information available on the last page of the article

thermodynamical stability and a low concentration of defects because the point defect formation energy of alumina is known to be large, especially for charged defects [6]. However, alumina is susceptible to breakaway corrosion due to consuming the aluminum reservoir in the alloy after long thermal exposure times. This phenomenon has been substantiated through extensive lifetime modeling [7].

The effects of Reactive Elements (REs) on the oxidation process and on the formed oxide layer have been studied extensively over the past decades [8–13], and it has been found that REs, for example, (1) improve scale adhesion, i.e. alumina scale adhesion to FeCrAl alloy. The role of RE in scale adhesion has been investigated by many researchers, and they suggest, for example, that the formation of oxide pegs, which its formation was facilitated by RE doping, has a role in adhesion enhancement [14, 15]. Another perspective, based on poisoned interface model (PIM), suggests that RE segregates to the scale/alloy interface, pinning the climb of misfit dislocation required for the scale growth [16]. James's comprehensive review summarized all possible factors affecting scale adhesion [17]. (2) reduce the parabolic growth, and (3) hinder the outward diffusion of cation ions [18, 19]. The advantages offered by REs are believed to stem from their large ion size and high oxygen affinity [16, 20, 21]. Also, RE distribution and concentration determine their impact [11]. Most of the recent works suggest that the RE concentration has to be lower than the solubility limit in the alloy, i.e. around a few hundred parts per million [17, 22–24]. Overdoping, however, can generate disadvantageous effects, for instance, formation of a second phase such as yttrium aluminum oxide ($Y_3Al_5O_{12}$ -YAG) [25, 26]. Also, high amounts of yttrium cause Y-rich oxide particles to form at alumina Grain Boundaries (GBs), which has a detrimental effect on scale adhesion by enabling micro-cracks and voids [11, 27].

While alumina grows mainly by inward diffusion [28], confirmed using ^{18}O tracer measurements [18, 19, 23], protective alumina scales on FeCrAl alloys have long to involve two layers: an inner layer comprising columnar grains and an outer layer with essentially an equiaxed grain structure [19, 29–33]. The presence of RE-rich oxide along the GB and at the outer surface of the scale is considered conclusive evidence of outward diffusion of cations [21, 34]. Such outward diffusion of cations is driven by the gradient in oxygen chemical potential across the scale. Eventually, over time, the concentration gradient is inversely related to the thickness of the oxide [29]. So, the composition of the new oxide formed in surface GB as a function of time and alumina scale thickness can give quantitative data on the magnitude of the GB flux and aluminum diffusivity.

Quantitative calculations of the GB flux of Al, based on the volume formed in surface GBs upon reoxidation of several relatively low RE-doped alloys [35, 36], agreed with Fick's 1st law, that is, the molar flux due to diffusion was proportional; to the concentration gradient. This paper will discuss FeCrAl overdoped with REs (specifically, Zr and Hf) from the point of view of elemental outward segregation of thermally grown alumina scales, which could give an insight into the lifetime of these alloys. For this purpose, atom probe tomography (APT) has been employed, as it allows for 3-D mapping of atoms in the oxide scale at near-atomic resolution. Transmission electron microscopy (TEM) was employed to correlate the results from both.

Experimental Procedures

Sample Preparation and Exposure

The samples were prepared from purity-high elements by arc melting technique under a protective Ar gas atmosphere. The compositions were determined by Spark-Optical Emission Spectrometry (Spark-OES) for Fecralloy™ & FeCrAl–Zr and Energy-Dispersive Spectroscopy (EDS) for Fecralloy™, FeCrAl–Zr & FeCrAl–Hf, the results are given in Table 1. In both samples, the Zr and Hf levels exceed the optimum amount of REs in alloys, which typically is around 0.05 at.%.

The samples were sectioned using a diamond wire saw with a thickness of 2.5 mm, then annealed in air at 1200 °C for 24 h for homogenization. The samples were polished with abrasive SiC paper down to 4000-grit, then using oil-base diamond suspension down to 1 µm and ultrasonically cleaned in alcohol and distilled water for 10 min.

Initial high-temperature oxidation exposures to form an adherent alumina scale were carried out in a chamber furnace in laboratory air at 1100 °C for 200 h, followed by cooling to room temperature in air, and measurements were made of the oxide layer thicknesses. Following Tolpygo and Clarke [37], the end of one side of these preoxidised specimens was subjected to taper grinding at an angle of 0.08° to form a wedge shape in which the outer equiaxed layer of scale was removed to reveal the columnar grains of the inner layer. This taper polishing was done using oil-based diamond, starting with 1 µm, down to 0.04 µm particle size using colloidal silica, followed by cleaning for 10 min in an ultrasonic bath. These modified specimens were oxidized for a further cycle at 1100 °C, and measurement of the new outward-growing oxide that was associated with the grain boundaries of the exposed original inner layer (as oxide ridges) was used to quantify the outward diffusion of Al. The stages in this procedure are illustrated schematically in Fig. 1. The optimum conditions to grow measurable oxide ridges in the second exposure were found to be 60 min for Fecralloy™, 20 min for FeCrAl–Zr, and 40 min for FeCrAl–Hf.

Analytical Techniques

The oxide scales on Fecralloy™ and FeCrAl–Zr were investigated by means of scanning electron microscopy/focused ion beam (SEM/FIB), transmission electron microscope (TEM), and laser-assisted atom probe tomography (APT). After the second exposure, the FeCrAl–Hf sample had significant spallation and cracks

Table 1 Alloys composition as analyzed by ICP-OES/EDS

Alloy/Compositions (at. %)	Fe	Al	C	Cr	Mn	Si	Y	Zr	Hf
Fecralloy™ (OES)	67.4	9.65	0.07	22.03	0.19	0.56	0.06	0.06	–
FeCrAl–Zr (OES)	66.5	10.27	0.3	22.45	–	–	–	0.5	–
FeCrAl–Hf (EDS)	66.8	9.64	0.3	22.74	–	–	–	–	0.52

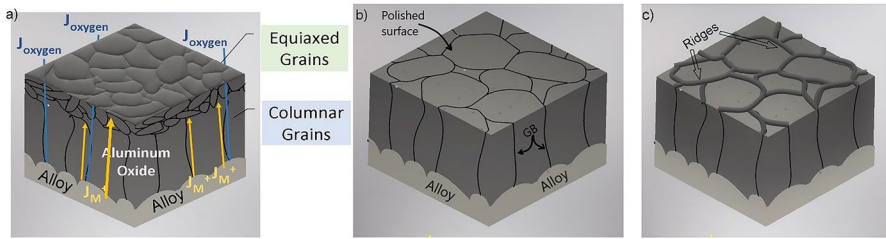


Fig. 1 Schematic illustration of the experimental procedures used to observe the outward growth of Alumina due to Al outward GB diffusion **a** typical alumina oxide structure after first oxidation. **b** After the first oxidation, the sample was polished by removing a portion of the formed oxide layer. **c** Re-oxidation after taper polishing

in most of the regions of interest, so TEM and APT were not employed in this condition. The specific instrumentation used for SEM/FIB was a Zeiss Auriga 60), for TEM an FEI Thermo Fisher Themis Z, and for APT a CAMECA LEAP 4000 XHR. The latter is equipped with a UV laser (wavelength 355 nm) and has a spot size less than 1 μm . TEM and APT samples were prepared using SEM/FIB with a maximum accelerating voltage of 30 kV for thinning steps, and a maximum accelerating voltage of 2 kV to minimize Ga ion damage to the sample.

The initial preparation of TEM and APT samples was very similar, from the creation of a lamella containing alumina grain boundaries, to attaching the lamella to a Micro-Post/TEM grid [38, 39]. Needle-shaped APT specimens with a shank angle of about 10° and an apex radius of less than 100 nm were prepared by the lift-out technique. Oxide samples containing grain boundary oxide were aligned approximately parallel to the field evaporation direction. The importance of attaining this particular APT sample shape is to acquire a high electric field (of the order of 10^{10} V/m [40]), to induce the removal of a conductive emitter surface atom as an ion. In case of materials like alumina with poor electrical conductivity, a combination of ultra-short laser pulses and high electrical voltage is used [41]. The sample tips were analyzed by APT at a temperature of ~ 35 K, a UV-laser pulse frequency of 125–200 kHz with a laser pulse energy of 30–40 pJ, and a detection rate of 0.25%. Reconstruction of the atom probe data was performed using AP Suite 6 software, based on the tip evolution profile. 3D atom distribution, 1D concentration profile across GB and interface, and proxigram analysis, which is a concentration of selected element as a function of distance to the iso-concentration surface, were employed [42]. The Thermo-Fisher Themis-Z was operated in the S/TEM mode at an accelerating voltage of 300 keV. Both bright-field (BF) and high-angle annular dark-field (HAADF) image modes were used.

The quantitative measures of solute segregation present at interfaces, commonly calculated using the methods proposed by Krakauer and Seidman [43], often reduce the characterization to a single value, i.e., the Gibbsian interfacial excess. The Gibbsian interfacial excess value Γ has been calculated, which indicates the solute atoms at internal interfaces. It is defined as [43]:

$$\Gamma_i = N_i^{\text{excess}}/A = (1/A)(N_i^{\text{vol}} - N_i^\alpha - N_i^\beta) = (1/A)N^{\text{vol}} \left[C_i^{\text{vol}} - C_i^\alpha \xi - C_i^\beta (1 - \xi) \right] \tag{1}$$

where N_i^{excess} is the excess number of atoms at an interface, A is the interfacial area over which Γ_i is determined. N_i^α and N_i^β are the number of atoms in α -phase and β -phase adjacent to the interface, ξ is the Gibbs dividing surface, and C represents the concentration of an element i in phase α or phase β [44].

Grain Boundary Outward Aluminum Flux

Oxide ridge volume measurements were obtained after the second oxidation using SEM/FIB. After sectioning through the oxide at 0°, the SEM stage was tilted to 54° in order to measure the cross-sectional area of the ridge A_{ridge} . By assuming that outward diffusion along an isolated grain boundary occurs without any lateral ‘leakage’ of atoms from grain boundaries to adjacent grains, the alumina grain boundary flux (J_{Al} is defined as the number of ions per length and time t), can be calculated using the relationship [45]:

$$J_{\text{GB}}^{\text{Al}} = \frac{N_{\text{GB}}^{\text{Al}}}{L_{\text{GB}} \cdot t} \tag{2}$$

where L_{GB} is the lateral length of the GB, $N_{\text{GB}}^{\text{Al}}$ is the number of segregated Al atoms along GB, where $N_{\text{GB}}^{\text{Al}}$ can be obtained from the measured grain boundary ridge volume $V_m = A_{\text{ridge}} \cdot L_{\text{GB}}$. The unit cell volume of $\alpha\text{-Al}_2\text{O}_3$ (V_{unitcell}) is 0.254 nm³ and with the number of Al ions per unit cell of $\alpha\text{-Al}_2\text{O}_3$ ($N_{\text{unitcell}}^{\text{Al}}$) being 12. This yields:

$$N_{\text{GB}}^{\text{Al}} = \frac{V_m}{V_{\text{unitcell}}} N_{\text{unitcell}}^{\text{Al}} \tag{3}$$

inserting Eq. (3) into Eq. (2), the aluminum GB flux can be determined as follows:

$$J_{\text{Al}} = \frac{12A_{\text{ridge}}}{V_{\text{unitcell}}} \left[\frac{\text{atm}}{\text{nm s}} \right] \tag{4}$$

Results

Oxide Scale Microstructure and Composition (SEM)

After an initial 200 h of oxidation at 1100 °C, the average external oxide scale thickness of Fecralloy™, FeCrAl–Zr, and FeCrAl–Hf was measured from three different samples and at a tenth different position, and it was found to be 3.1 ± 0.3 μm, 5.6 ± 2.7 μm, and 4.9 ± 2.2 μm, respectively. Figure 2 shows SEM images of the cross sections of the oxidized samples. Whereas Fecralloy™ did not form internal oxides, quite extensive internal oxidation had occurred on both FeCrAl–Zr and FeCrAl–Hf samples to average depths of 79.2 ± 3.2 μm and 18.2 ± 2.2 μm, respectively.

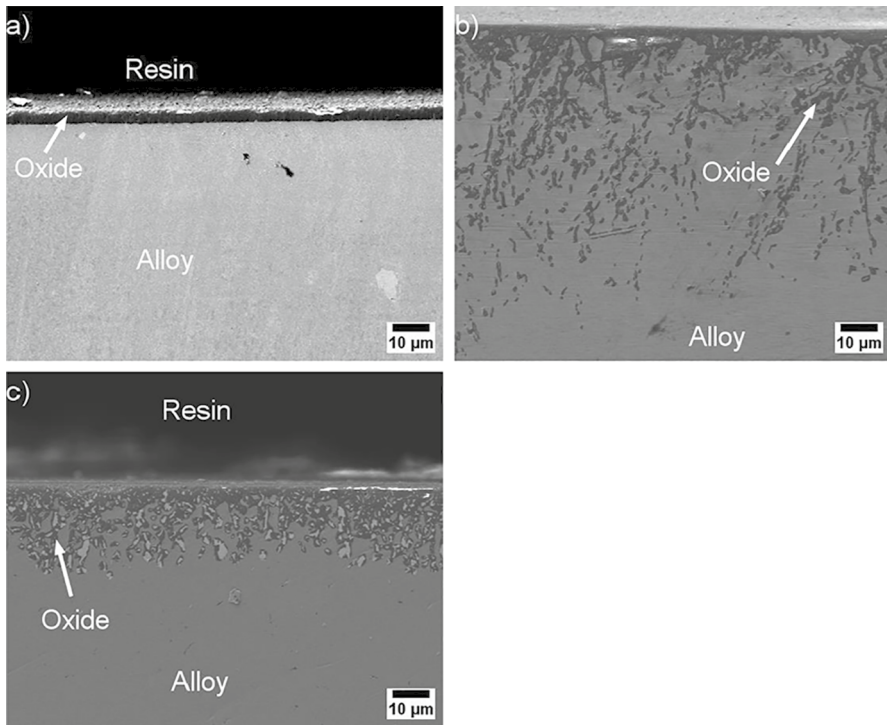


Fig. 2 Secondary electron images of the samples after first oxidation for 1100 °C for 200 h. **a** FeCrAlloy™, **b** FeCrAl–Zr, **c** FeCrAl–Hf

Topographies using SEM of the surface of FeCrAl–Hf after bevel polishing and re-oxidation in the second exposure are shown in Fig. 3. While a layer of transient Fe-rich scale had formed, most of it had spalled extensively to expose partially spalled alumina (Fig. 3b) which exhibited ridges (Fig. 3c), indicating that transport of cations along alumina grain boundaries had occurred. Distinct areas of Hf oxide were present in some areas from which the alumina had spalled (Fig. 3d). Topographies of the scales formed on FeCrAlloy™ and FeCrAl–Zr after the same re-exposure, shown in Fig. 4, illustrate new alumina ridges formed over grain boundaries in the alumina scale.

Oxide Scale and Composition (TEM)

After the second exposure, high-resolution electron imaging by TEM/STEM was performed on the FeCrAlloy™ and FeCrAl–Zr specimens. The FeCrAl–Hf specimens were not examined due to the severe scale spallation that had occurred.

Figure 5 shows the elemental maps of Fe, Cr, and Zr ions for FeCrAlloy™. The atomic fraction at the oxide layer for Fe ranges between 4.05×10^{-4} to 3.3×10^{-3} , Cr between 4.53×10^{-5} to 2.1×10^{-3} and Zr between 5.3×10^{-5} to 3×10^{-3} , meaning

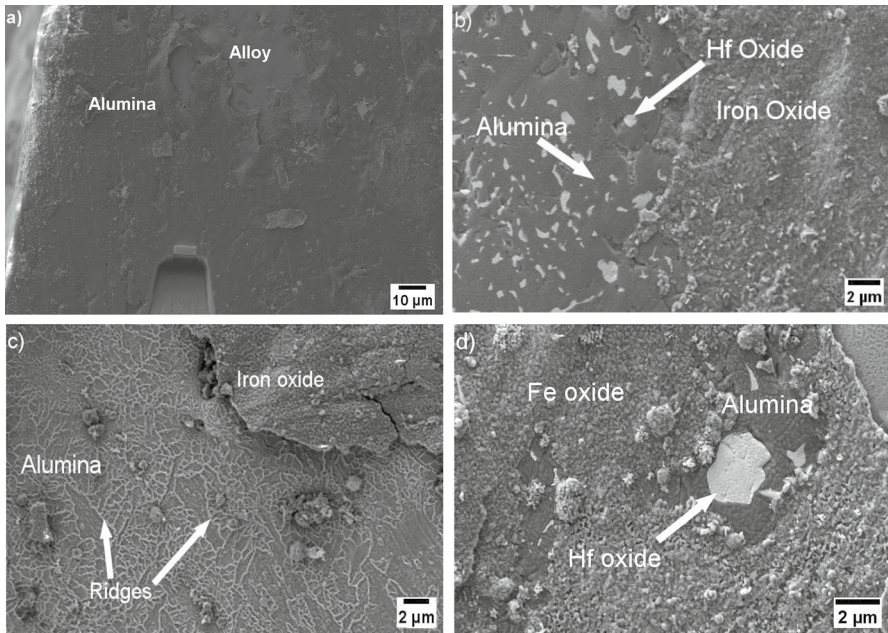


Fig. 3 SEM topographies of scales formed on FeCrAl-Hf after the second oxidation exposure (1100 °C for 40 min): **a** low-magnification image showing thin alumina scale with areas of spallation. **b** Higher-magnification image showing alumina scale and areas of Hf oxide exposed after spallation of outer Fe-rich scale. **c** Oxide ridges on alumina beneath spalled Fe-rich scale; and **d** alumina and relatively large area of Hf oxide revealed beneath spalled external Fe-scale

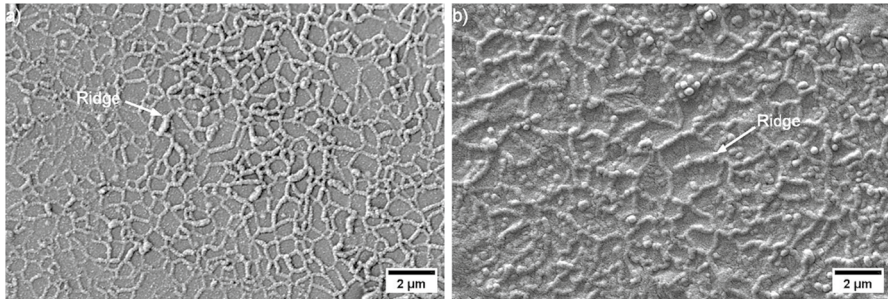


Fig. 4 SEM micrograph of **a** Fecralloy™. **b** FeCrAl-Zr (overdoped), after second thermal exposure for 60 min, and 20 min, respectively. Both SEM images show Alumina oxide ridges formed on top alumina GBs

nearly no segregation to the oxide layer. The cross-sectional HAADF-STEM image of the oxide scale grown on the FeCrAl alloy overdoped with Zr (FeCrAl-Zr) and EDX elemental mapping images are shown in Fig. 6.

As Fig. 6b, there was an indication of a Cr-enriched region within the alumina layer. The 1D concentration profile (Fig. 6c) demonstrates a relatively sudden

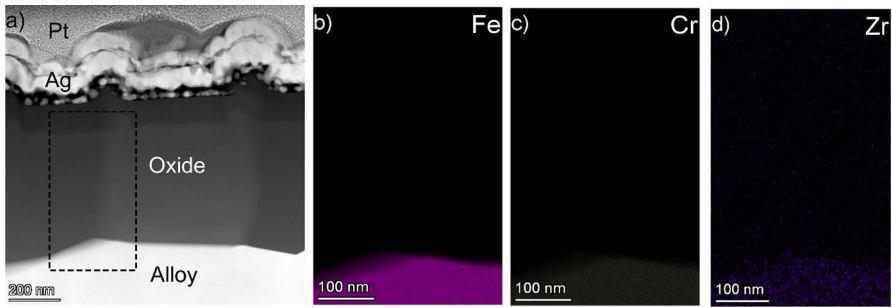


Fig. 5 **a** HAADF-STEM image of the oxide layer grown on Fecralloy™ after the second exposure. **b–d** EDS maps of Fe, Cr, and Zr ions, respectively. EDS maps showing a segregation of Zr ions to the oxide layer

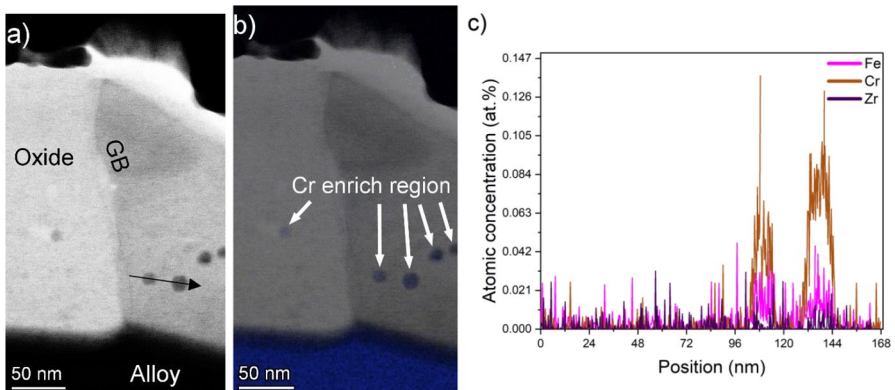


Fig. 6 **a** The oxide scale formed on FeCrAl-Zr alloy after the 2nd thermal exposure. **b** Elemental map shows the distribution of Cr ions. **c** 1D concentration profile along the indicated direction in **(a)**

increase in Cr concentration in the indicated region in Fig. 6a by an arrow. Further investigation of GBs in the alumina scale detected Zr segregation to the oxide grain boundaries (Fig. 7) reaching a concentration of 7.27 at%.

Atom Probe Tomography (APT)

APT was used to examine the microstructure in greater detail and gain a better understanding of the distribution of the atoms in the oxide scale. APT analyses were made of samples from newly grown ridges, including the GB beneath it, on Fecralloy™ and FeCrAl-Zr, and from the oxide-alloy interface of FeCrAl-Zr after the second oxidation exposure. Elemental enrichment of these characteristics often allows APT to monitor the grain boundaries, and Fig. 8 shows reconstructed 3-D atom probe tomography images of a tip-sample (containing part of an alumina grain

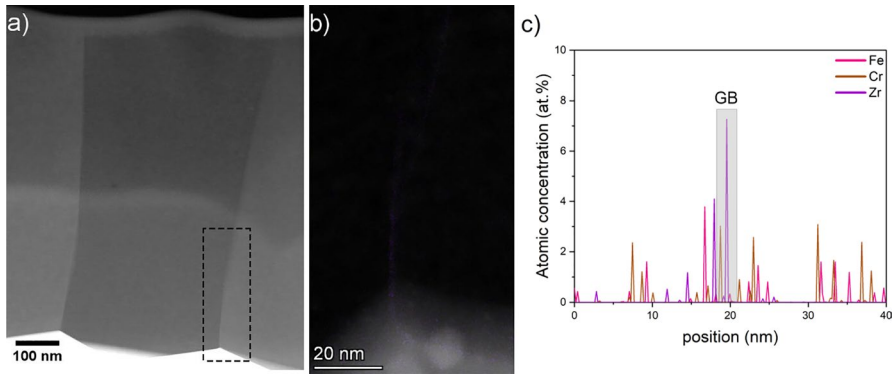


Fig. 7 **a** STEM-HAADF image of alumina scale for FeCrAl-Zr sample. **b** EDS map across the alumina GB showing a segregation of Zr ion along alumina GB (**c**)

boundary) farthest from the new oxide ridge grown on FecralloyTM. The location of the grain boundary is indicated in Fig. 8c, based on one-dimensional C ion enrichment. The APT analysis of the alumina grown on FecralloyTM did not reveal any discernible patterns (such as segregation at grain boundaries or segregation to the oxide layer), based on the atomic distribution of Fe or Cr ions present in the alloy.

A further APT sample of FecralloyTM was taken from a sample of the alumina grain boundary nearest to the oxide ridge (near the oxide/air interface), Fig. 9a. Fe was found in the grain boundaries of the alumina layer close to the oxide/air interface, as indicated in Fig. 9b, which also shows the spatial distribution of part of the deposited silver layer, O ions, and Al ions. Figure 9c and d shows the atomic density maps for Fe and Cr at the indicated location in Fig. 9a. It can be seen that the Fe is segregated along the GB to the oxide/gas interface. Also, there are traces of Cr in the vicinity of the same region. The Gibbsian interfacial excess of Fe (FecralloyTM sample) at the alumina oxide GB was calculated and it was $\Gamma_{\text{Fe}}^{\text{GB}} = 0.42 \text{ nm}^{-1}$.

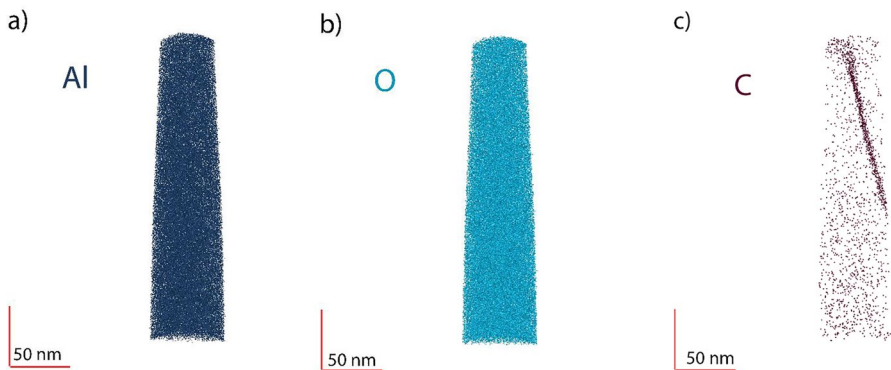


Fig. 8 APT reconstruction elemental maps of a tip-sample from oxide scale grown on FecralloyTM

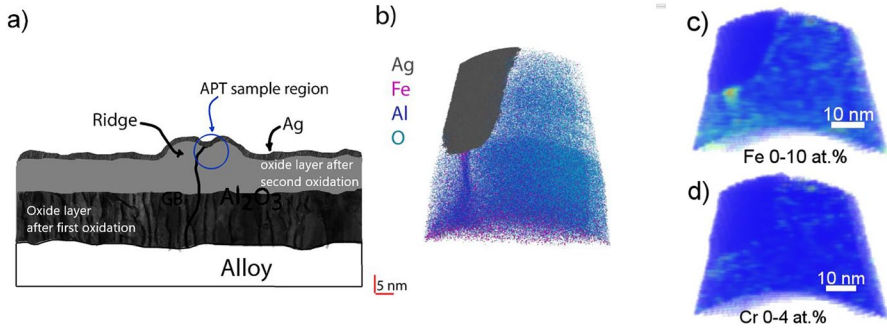


Fig. 9 **a** The location from which the APT sample was prepared. **b** Reconstructed 3-D APT images showing atomic distribution of Fe, Al, O and Ag on FeCrAlloyTM. **c** and **d** Atomic density maps of Fe and Cr

In the case of FeCrAl–Zr, two APT samples of oxide scale containing GBs and a sample containing an oxide-alloy interface were successfully prepared. As shown in Fig. 10a and b, the isosurface map of Fe and 3D atomic distribution of Cr indicated a triple junction point at the oxide-alloy interface, which represents the intersection point of adjacent oxide grain and the oxide/alloy interface. The triple junction point was confined between the alloy and two oxide grains and was identified by its hump-like location and shape (e.g., Figs. 5a, 8a show the same hump-like at the triple junction point). The emergence of a Fe-rich band (Fig. 10a) and a Cr-rich band (Fig. 10b) above and close to the alumina GB were thought to be signs of Cr and Fe ion segregation as a result of over doping.

Additionally, the presence of Fe and Zr precipitates near the grain boundary may increase the segregation of Fe and Zr ions along it. The profiles of local

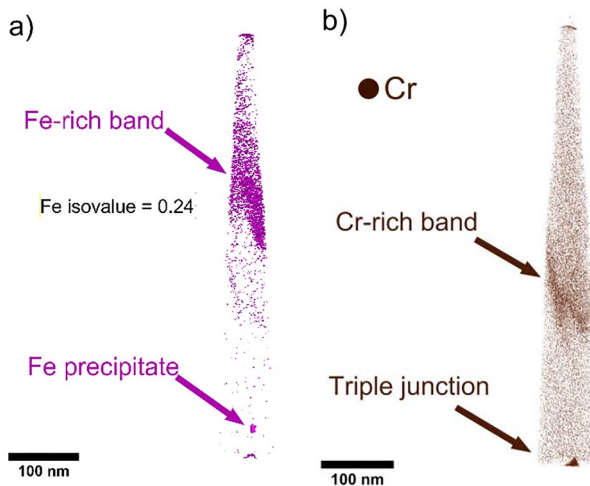


Fig. 10 **a** APT reconstructed isosurface maps of Fe in oxide layer grown on FeCrAl–Zr tip-sample after the 2nd exposure for 20 min. **b** atom distribution of Cr

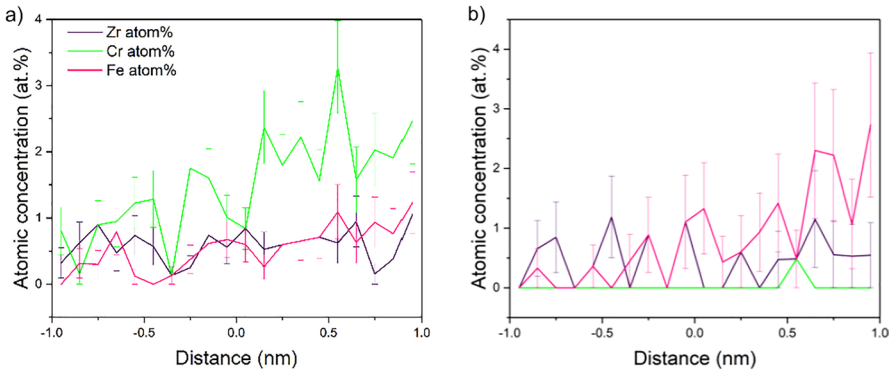


Fig. 11 Proximity histograms (proxigrams) of **a** Triple junction point. **b** Fe precipitate

atomic concentrations vs. proximity to the triple junction point in FeCrAl–Zr (proximity histogram, or ‘proxigram’) shown in Fig. 11a allow the relative concentrations of Zr, Cr, and Fe to be compared. These indicate that Cr (3.3 at%) is more prevalent than Fe or Zr. The 1-D concentration profiles taken from the grain boundary exhibit a sudden increase in Zr concentration, see Fig. 12b. The Gibbssian excess of Zr for the regions of interest (ROIs) in Fig. 12a was calculated to be $\Gamma_{Zr}^{GB} = 0.7 \text{ nm}^{-2}$. Since the Gibbssian excess of Zr in FeCrAl–Zr is higher than Gibbssian excess Fe in FeCrAlloy™, and the ionic size of Zr is higher than Fe, this suggests an enhancement of segregation and an increase in GB width.

APT tip-sample from the FeCrAl–Zr sample containing an oxide-scale interface yielded the 3-D atom maps of the distribution of Fe, Cr, Zr, Al, and O shown in Fig. 13. The data in Fig. 13c infer that Zr ions are segregated to the oxide

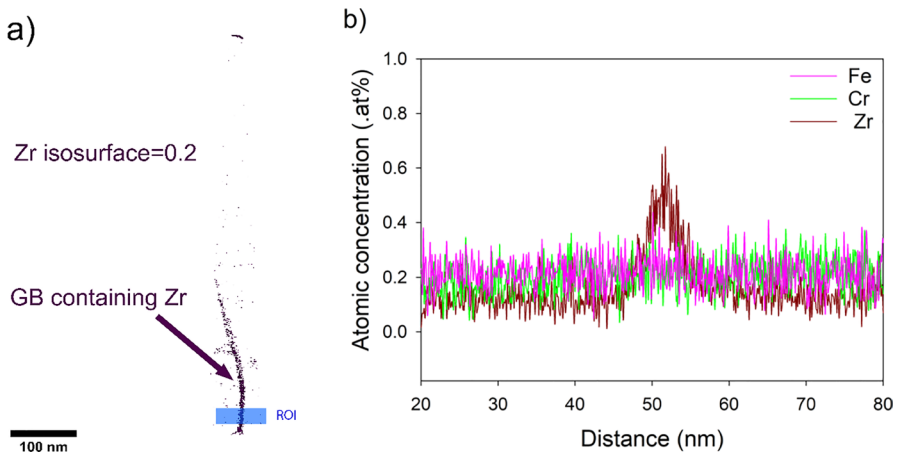


Fig. 12 **a** 3-D APT reconstructed analyses for a tip sample from FeCrAl–Zr, showing grain boundaries and the regions of interest (analysis was made in the Z-direction). **b** 1-D concentration profile on a grain boundary

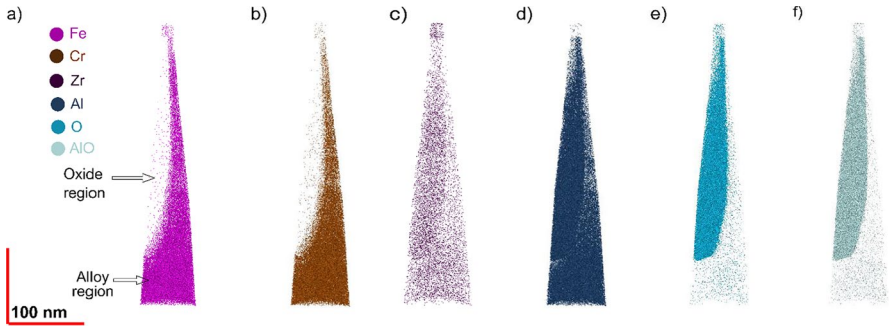


Fig. 13 3D elemental map distribution in APT tip-sample of FeCrAl–Zr containing oxide/alloy interface. **a** Fe. **b** Cr. **c** Zr. **d** Al. **e** O. **f** AlO

layer. As indicated, these were generated at four segments along the oxide alloy interface. In particular, the maximum value of the atomic concentration of Fe occurred in the alloy region of ID6.

Based on the curve of the interface near the bottom of the 3-D elemental map for Fe (Fig. 13a), this location appears to be near a triple junction region. Figure 14 indicates the change in concentration of these elements across the oxide-alloy interface. On average, Fe was present at a level of 29.22 at. % in the oxide-alloy interface but only 1.24 at% in the oxide grain. The corresponding levels for Cr were 6.12 at. % and 0.39 at. %, while the level of Zr in the alloy and oxide was the same (0.097 at% and 0.11 at%, respectively).

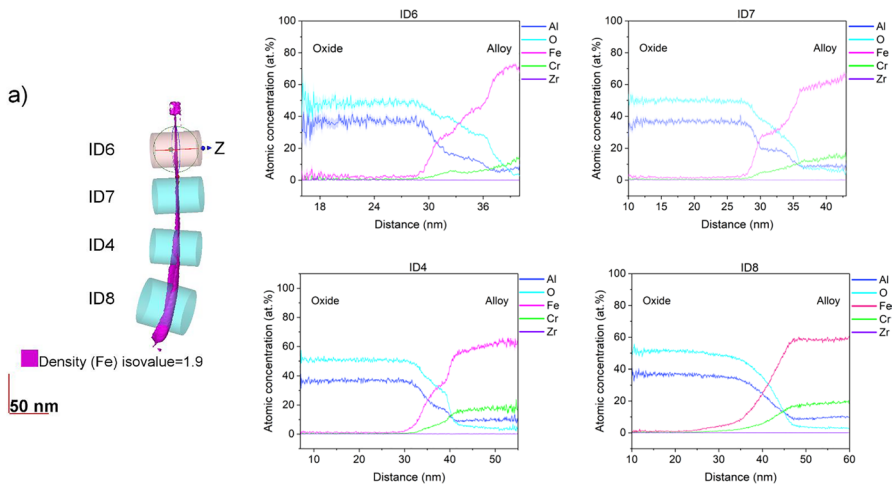


Fig. 14 APT analysis of oxide/alloy interface region of FeCrAl–Zr sample after 2nd isothermal oxidation at 1100 °C in air for 20 min. **a** Fe isosurface used to highlight the interface region. (ID4–ID8) corresponding 1D concentration profile showing the segregation behavior of Al, O, Fe, Cr, Zr ions through oxide/alloy interface

Outward Flux of Al Along Alumina GB

The data acquired for the flux of aluminum along alumina GB is shown in Fig. 15a, which is plotted using a double-logarithmic of the oxide thickness against the Al flux along GB, using Eq. 4. Very good agreement was found with results published by Nychka and Clarke [35], shown in Fig. 15b. The results for alloys FeCrAlloy™ and FeCrAl–Zr followed Fick’s law of diffusion. From Fig. 15a, it can be deduced that the flux of Al along GB has enhanced in overpored FeCrAl with Zr.

Discussion

The methodology of sample preparation and quantifying the Al flux along oxide GB was based on the second polishing step and tuning of the second oxidation time to produce a specific (ridged) microstructure on the oxide surface, where its growth is time and oxide thickness-dependent. The second polishing is considered a critical stage, but it is also a contentious step since polishing could introduce additional dislocation, and subsequently, yield a higher flux. To reduce this effect, the second polishing should be performed using as small as possible polishing particle size and for at least 11 min. Other milling techniques reportedly [36] have disadvantages that affect the Al flux. With Xe gas milling, for instance, Xe ions can impede oxide grain boundaries, consequently hindering Al segregation along them. Mechanically-polished Hf-doped samples exhibited a higher flux for the same species, compared to Xe-milling of the same samples.

The straightforward formula to evaluate the flux along oxide GBs disregards several factors that could affect the results, e.g., low-, and high-angle GBs are not addressed in Eq. 4, even though these two factors have an impact on segregation. The leakage of atoms from GBs to adjacent grains was also disregarded. However, Eq. 4 can serve its purpose by giving an estimated value of Al flux along GBs. The results of the present work correlate well with Nychka and Clarke’s results (Fig. 15b) and comply with the 1st Fick law of diffusion.

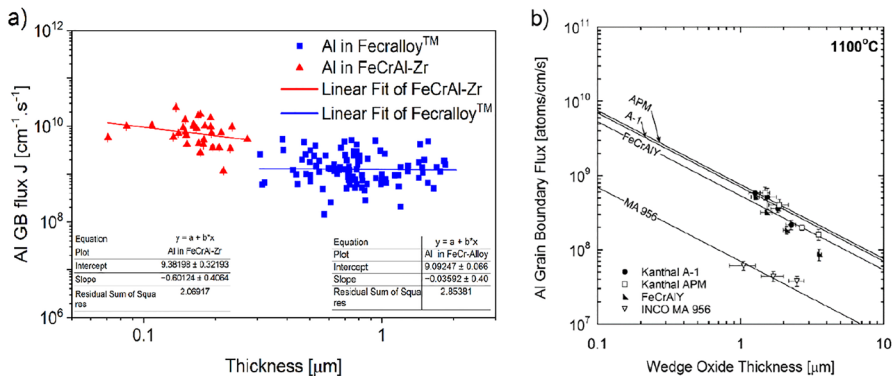


Fig. 15 Grain boundary flux of aluminum versus wedge oxide thickness for **a** FeCrAlloy™ and FeCrAl–Zr alloy after re-oxidation for 1 h and 20 min, respectively, and **b** Data for several alloys pre-oxidized for 120 h at 1100 °C in air, and re-oxidized for 4 h at 1100 °C in air [35]

Earlier studies have demonstrated that the presence of RE(III) elements leads to a notable expansion in grain boundary width as the ionic radius and concentration increases. This expansion generates accumulated stress, facilitating the rapid precipitation of RE oxides, and in some cases leads to oxide spallation [46–48]. Numerous models have attempted to predict the effects of REs: the so-called poisoned interface model (PIM) [49] proposed that the REs and cation impurities segregate to the alloy/scale interface and react with the defects, having an impact on the oxide growth mechanism. However, the PIM model contradicts the findings in Pint's paper [31], where it lapses any role of RE doping in the scale. Furthermore, it does not consider the potential presence of small voids at oxide/alloy interface. The grain boundary segregation model proposed that the REs and cation impurities share the same defect routes for incorporation into oxide scale growth. Cation impurities tend, in general, to segregate at GBs the same as aliovalent cations, which requires vacancies or interstitials to preserve electric neutrality, which in turn increases the diffusivity in GBs [50]. The first mechanism of GB segregation model can be interpreted that the presence of REs at the GBs makes them act as site blockers to the other cation impurities, hence reducing its segregation. The other postulation of that model is the swamping-out mechanism [51], supported experimentally using HRTEM and STEM energy dispersive X-ray analysis [52]. In that mechanism, isovalent segregants (e.g., Y^{+3}) swamp out Si and Ca impurities. The aliovalent cation segregation can enhance the GB diffusivity of Al cations and O anions by increasing the anion and cation vacancies. The recent trend to explain the effect of the RE relies on the band structure of Al_2O_3 scales [53–56], where the electrons and holes play a role in the scaling reaction (i.e., creation and annihilation of vacancies at interfaces). The participation of the electron or holes arises from near-band edge defect structure. Doping with reactive elements could alter the electronic structure, due to the segregation, and involve a migration of grain boundary disconnections; a class of GB ledge defects characterized by a step height h and a Burgers vector b , containing positively charged and negatively charged jogs [57, 58]. The increase in the amount of RE can increase the migration of disconnections. Eventually, this led to enhanced segregation.

The practical limits associated with the REs commonly used in commercial alloys were reported by several researchers [17, 22–24], and there was an agreement that the proper amount of the RE is several hundreds of ppm, and the amount itself differentiates from one RE element to another, but stayed in that range. These limits are related to the solubility limits of the REs and the presence of impurities, like S and C. Exceeding these limits would lead to the formation of second phases (Fig. 3b, d) or intermetallic compound with aluminum, spallation, and oxide layer failure.

The Fecralloy™ formed the thinnest oxide thickness with no internal oxidation after the first and second oxidation at 1100 °C, demonstrating the feasibility of RE addition when incorporated under defined conditions [11, 21]. The 3-D atom distribution maps acquired in this work from APT of alumina formed on Fecralloy™ after the 2nd thermal exposure (Figs. 8, 9) show data from sections of alumina grain boundaries: the area shown in Fig. 8 contains an alumina grain boundary farthest from the newly-formed oxide ridge, while that in

Fig. 9 represents an alumina grain boundary nearest to the ridge (near the oxide/air interface). The map in Fig. 9b shows Fe atoms detected at an alumina grain boundary. This contrasts with the absence of any notable segregation of Fe (or Cr) in the maps in Fig. 8. Presumably, the source of those Fe atoms was surface diffusion of Fe atoms that exists from the first oxidation process, which occupied 200 h.

The APT reconstruction analyses correlate with the STEM/EDS results (see Figs. 5, 8), as both indicated the absence of Fe or Cr ion segregation at alumina grain boundaries in the Fecralloy™ sample, which reflects the feasibility of the REs acting as site blocker of outward ion segregation.

It can be inferred from Fig. 15, and based on the SEM images, that the outward grain boundary diffusion of Al in FeCrAl–Zr was enhanced as a result of overdoping, contrary to the beneficial effect of REs on the outward diffusion of Al in the Fecralloy™ sample. Segregation of Fe and Cr ions was identified by the appearance in the oxide layer of bands rich in Fe and Cr ions, as indicated in the reconstructed elemental maps shown in Fig. 10. According to the simple theory of equilibrium segregation [59], increasing the amount of RE would raise the concentration of segregant at GB until it reaches the saturation concentration, leading to the formation of RE oxides [60]. Others [52] have proposed that increasing the amount of REs increases the disorder in the alumina lattice, allowing improved diffusion rate through the oxide [61].

After the second exposure of the FeCrAl–Zr sample, Zr ions were found to have segregated along oxide grain boundaries (see Figs. 7b, 12). The formation of a Cr-precipitate near the grain boundary could contribute to the segregation of Cr ions along grain boundaries. This points to a dynamic segregation and purification process of the alumina scale (see Figs. 10b, 6b, c) and surface energy minimization.

The level of overdoping of the FeCrAl–Hf alloy led to disastrous degradation of its ability to form a protective alumina scale. The alloy exhibited reduced oxide scale adhesion, and formation of a second phase oxide or intermetallic compound with Al that promoted internal oxidation by enhancing inward diffusion [9, 62], as illustrated in Figs. 3 and 5. The major undesirable effect was scale spallation, apparently promoted by the formation of HfO₂ at the alloy/scale interface, presumably due to differences in thermal expansion among the oxides [63, 64]. Additionally, the lattice mismatch between alumina and hafnia and the increased Pilling-Bedworth ratio upon hafnium oxidation are related. Hafnium has an extremely high affinity for oxygen [65] and tends to induce higher density of defects in alumina oxide compared to Zr, and this characteristic is evident in the formation of Hf oxide in FeCrAl–Hf sample and the formation of Fe oxides on the surface, as depicted in Fig. 3. Hf ion has a larger ionic radius and higher charge density make it more prone to introduce lattice distortion and create vacancies, which can act as charge carriers and affect the transport properties. Meanwhile, the solubility of oxygen in Hf is lower than it is in Zr, this may explain the higher oxidation depth in the FeCrAl–Zr sample (Fig. 2b).

Conclusions

The oxidation behavior of Fecralloy™ and FeCrAl overdoped samples with Hf or Zr was investigated using a novel technique involving reoxidation of an isothermally formed scale from which the outer layer of the alumina scale has been formed. The results can be summarized as follows:

1. The inward diffusion was enhanced in the overdoped samples where the inward diffusion is more enhanced by overdoping with Zr than overdoping with Hf based on the depth of internal oxidation.
2. Based on the thickness of the oxide scale formed on the overdoped alloys, outward diffusion of aluminium was enhanced (see the J values for the grain boundary flux of Al, Fig. 15).
3. In the overdoped FeCrAl with Zr, the Fe and Cr ion segregation within oxide grains was observed (Figs. 10a, b, 12), which may attributed to the overdoping effect or as a remnant of the transient stage. Additionally, the presence of Zr ions was detected within the oxide grain boundaries of the overdoped sample with Zr.
4. The sample overdoped with Hf experienced strong scale spallation after the second exposure, significantly higher than the Zr-overdoped sample. This precluded further analysis of this alloy.
5. The beneficial effects, including the hindered outward diffusion of Al and other constituents along the alumina grain boundaries, reducing the growth rate, and enhancing the adhesion of the alumina scale to the alloy, were observed in the Fecralloy™ sample. In contrast, the overdoped sample with Hf exhibited strong spallation after the second exposure, which was relatively much higher than in the overdoped sample with Zr.

Acknowledgements The authors would like to thank the German Academic Exchange Service (DAAD) scholarship. This work was carried out with the support of the Karlsruhe Nano Micro Facility (KNMFi, www.knmf.kit.edu), a Helmholtz Research Infrastructure at Karlsruhe Institute of Technology (KIT, www.kit.edu) (Project No. ha 2020-024-028730). Also, special thanks to Dr. Dinara Sobola and Prof. Dr.-Ing. Martin Heilmaier for the scientific discussion. The authors would like to thank CEITEC Nano Research Infrastructure for their assistance with this research.

Author contributions Samer Daradkeh wrote the main manuscript text, prepared figures, data collection and analysis. Torben Boll review the manuscript and data analysis. Oscar Recalde helped in data collection and analysis. All other Authors review the manuscript.

Funding Open access publishing supported by the National Technical Library in Prague.

Declarations

Conflict of interest The authors declare that they have no known competition for financial interests or personal relationships that could have appeared to influence the work reported in this paper.

Open Access This article is licensed under a Creative Commons Attribution 4.0 International License, which permits use, sharing, adaptation, distribution and reproduction in any medium or format, as long as you give appropriate credit to the original author(s) and the source, provide a link to the Creative Commons licence, and indicate if changes were made. The images or other third party material in

this article are included in the article's Creative Commons licence, unless indicated otherwise in a credit line to the material. If material is not included in the article's Creative Commons licence and your intended use is not permitted by statutory regulation or exceeds the permitted use, you will need to obtain permission directly from the copyright holder. To view a copy of this licence, visit <http://creativecommons.org/licenses/by/4.0/>.

References

1. M. Sundberg, G. Malmqvist, A. Magnusson, and T. El-Raghy, in *Ceramics International*, Vol. 30 (Elsevier, 2004), p. 1899.
2. E. A. Gulbransen and K. F. Andrew, *Journal of the Electrochemical Society* **106**, 294 (1959).
3. H. Josefsson, F. Liu, J.-E. Svensson, M. Halvarsson, and L.-G. Johansson, *Materials and Corrosion* **56**, 801 (2005).
4. C. Badini and F. Laurella, *Surface and Coatings Technology* **135**, 291 (2001).
5. C. Tang, A. Jianu, M. Steinbrueck, M. Grosse, A. Weisenburger, and H. J. Seifert, *Journal of Nuclear Materials* **511**, 496 (2018).
6. M. Kitayama, *The Wulff Shape of Doped and Undoped Alumina*, (University of California, 1996).
7. W. J. Quadakkers and M. J. Bennett, *Materials Science and Technology* **10**, 126 (1994).
8. S. Chevalier, *Materials and Corrosion* **65**, 109 (2014).
9. P. Y. Hou, *Materials Science Forum* **696**, 39 (2011).
10. B. A. Pint, J. R. Martin, and L. W. Hobbs, *Solid State Ionics* **78**, 99 (1995).
11. J. Quadakkers and L. Singheiser, *Materials Science Forum* **369–372**, 77 (2001).
12. J. Stringer, *Materials Science and Engineering A* **120–121**, 129 (1989).
13. H. Hindam and D. P. Whittle, *Journal of the Electrochemical Society* **129**, 1147 (1982).
14. J. Eklund, B. Jönsson, A. Persdotter, J. Liske, J. E. Svensson, and T. Jonsson, *Corrosion Science* **144**, 266 (2018).
15. R. Pendse and J. Stringer, *Oxidation of Metals* **23**, 1 (1985).
16. X. Wang, X. Peng, X. Tan, and F. Wang, *Scientific Reports* **6**, 1 (2016).
17. J. L. Smialek, *Oxidation of Metals* **97**, 1 (2022).
18. W. J. Quadakkers, H. Holzbrecher, K. G. Briefs, and H. Beske, *Oxidation of Metals* **32**, 67 (1989).
19. K. P. R. Reddy, J. L. Smialek, and A. R. Cooper, *Oxidation of Metals* **17**, 429 (1982).
20. C. Mennicke, E. Schumann, M. Rühle, R. J. Hussey, G. I. Sproule, and M. J. Graham, *Oxidation of Metals* 1998. <https://doi.org/10.1023/A:1018803113093>.
21. B. A. Pint, in *Proceedings of the John Stringer Symposium on High Temperature Corrosion* (Citeseer, 2003), p. 9.
22. F. Pedraza, R. Troncy, A. Pasquet, J. Delautre, and S. Hamadi, in *Superalloys 2020* (Springer; 2020), p. 781.
23. B. A. Pint, *Journal of the American Ceramic Society* **86**, 686 (2003).
24. A. W. Funkenbusch, J. G. Smeggil, and N. S. Bornstein, *Metallurgical Transactions A* **16**, 1164 (1985).
25. R. Cuffe, H. Buscail, E. Caudron, F. Riffard, C. Issartel, and S. el Messki, *Applied Surface Science* **229**, 233 (2004).
26. N. Mortazavi, C. Geers, M. Esmaily, et al., *Nature Materials* **17**, 610 (2018).
27. G. Gottstein, *Physical Foundation of Material Science. Nature* (2004), p. 282.
28. J. Engkvist, U. Bexell, M. Grehk, and M. Olsson, *Materials and Corrosion* **60**, 876 (2009).
29. F. N. Rhines and J. S. Wolf, *Metallurgical Transactions* **1**, 1701 (1970).
30. F. A. Golightly, F. H. Stott, and G. C. Wood, *Oxidation of Metals* **10**, 163 (1976).
31. B. A. Pint, *Oxidation of Metals* **45**, 1 (1996).
32. E. Wessel, V. Kochubey, D. Naumenko, L. Niewolak, L. Singheiser, and W. J. Quadakkers, *Scripta Materialia* **51**, 987 (2004).
33. T. Huang, D. Naumenko, P. Song, J. Lu, and W. J. Quadakkers, *Oxidation of Metals* **90**, 671 (2018).
34. V. K. Tolpygo and D. R. Clarke, *Materials at High Temperatures* **20**, 261 (2003).
35. J. A. Nychka and D. R. Clarke, *Oxidation of Metals* **63**, 325 (2005).
36. T. Boll, K. A. Unocic, B. A. Pint, A. Mårtensson, and K. Stiller, *Oxidation of Metals* **88**, 469 (2017).

37. V. K. Tolpygo and D. R. Clarke, *Evidence of Outward Aluminum Grain-Boundary Diffusion in Y- and Zr-Doped Alumina Scales*, *High Temperature Corrosion and Materials Chemistry* (The Electrochemical Society, 1999), p. 99.
38. A. Cerezo, P. H. Clifton, M. J. Galtrey, et al., *Materials Today* **10**, 36 (2007).
39. S. D. Rao, K. Muraleedharan, and C. J. Humphreys, *Microscopy: Science, Technology, Applications and Education* **2**, 1232 (2010).
40. Y. M. Chen, T. Ohkubo, and K. Hono, *Ultramicroscopy* **111**, 562 (2011).
41. M. K. Miller and R. G. Forbes, in *Atom-Probe Tomography: The Local Electrode Atom Probe* (2014), p. 9781489974.
42. J. T. Sebastian, J. Rüsing, O. C. Hellman, et al., *Ultramicroscopy* **89**, 203 (2001).
43. B. W. Krakauer and D. N. Seidman, *Physical Review B* **48**, 6724 (1993).
44. M. K. Miller and G. D. W. Smith, *Applied Surface Science* **87–88**, 243 (1995).
45. T. Boll, K. A. Unocic, B. A. Pint, and K. Stiller, *Microscopy and Microanalysis* **23**, 396 (2017).
46. T. L. Barth, P. K. Weber, T. Liu, et al., *Corrosion Science* **209**, 110798 (2022).
47. V. Babic, C. Geers, and I. Panas, *Oxidation of Metals* **93**, 229 (2020).
48. B. A. Pint, A. J. Garratt-Reed, and L. W. Hobbs, *Journal of the American Ceramic Society* **81**, 305 (2005).
49. P. Pieraggi, *Materials Science Forum* **251–254**, 299 (1997).
50. T. Yokoi, M. Yoshiya, and H. Yasuda, *Scripta Materialia* **102**, 91 (2015).
51. T. Nakagawa, I. Sakaguchi, N. Shibata, et al., *Acta Materialia* **55**, 6627 (2007).
52. T. Gemming, S. Nufer, W. Kurtz, and M. Rühle, *Journal of the American Ceramic Society* **86**, 590 (2003).
53. M. Wada, T. Matsudaira, and S. Kitaoka, *Journal of the Ceramic Society of Japan* **119**, 832 (2011).
54. T. Matsudaira, M. Wada, T. Saitoh, and S. Kitaoka, *Acta Materialia* **59**, 5440 (2011).
55. T. Matsudaira, M. Wada, T. Saitoh, and S. Kitaoka, *Acta Materialia* **58**, 1544 (2010).
56. S. Kitaoka, T. Matsudaira, and M. Wada, *Materials Transactions* **50**, 1023 (2009).
57. A. H. Heuer, T. Nakagawa, M. Z. Azar, et al., *Acta Materialia* **61**, 6670 (2013).
58. A. H. Heuer, M. Zahir Azar, H. Guhl, et al., *Journal of the American Ceramic Society* **99**, 733 (2016).
59. Ed. Hondros, Mr. Seah, S. Hofmann, and P. Lejček, in *Physical Metallurgy* (Elsevier, 1996), p. 1201. <https://doi.org/10.1016/B978-044489875-3/50018-1>.
60. F. Wakai, T. Nagano, and T. Iga, *Journal of the American Ceramic Society* **80**, 2361 (1997).
61. J. Klöwer, *Materials and Corrosion* **51**, 373 (2000).
62. D. P. Whittle and J. Stringer, *Philosophical Transactions of the Royal Society of London. Series A, Mathematical and Physical Sciences* **295**, 309 (1980).
63. F. H. Stott, *Materials Science Forum* **251–254**, 19 (1997).
64. C. Leyens, B. A. Pint, and I. G. Wright, *Surface and Coatings Technology* **133–134**, 15 (2000).
65. S. Grigoriev, A. Vereschaka, V. Uglov, et al., *Wear* **518–519**, 204624 (2023).

Publisher's Note Springer Nature remains neutral with regard to jurisdictional claims in published maps and institutional affiliations.

Authors and Affiliations

Samer I. Daradkeh^{1,2,3} · Oscar Recalde⁴ · Marwan S. Mousa⁵ · Dinara Sobola^{3,6} · Torben Boll^{2,7}

✉ Samer I. Daradkeh
252679@vutbr.cz

¹ Central European Institute of Technology, Brno University of Technology, Purkyňova 656/123, 612 00 Brno, Czech Republic

² Institute for Applied Materials – Materials Science and Engineering (IAM-WK), Karlsruhe Institute of Technology (KIT), Engelbert-Arnold-Str. 4, 76131 Karlsruhe, Germany

³ Department of Physics, Faculty of Electrical Engineering and Communication, Brno University of Technology, Technická 2848/8, 616 00 Brno, Czech Republic

- ⁴ Advanced Electron Microscopy Division, Department of Materials- and Earth Science, Technical University of Darmstadt, Darmstadt, Hessen, Germany
- ⁵ Department of Physics, Mu'tah University, Al-Karak 61710, Jordan
- ⁶ Institute of Physics of Materials, Czech Academy of Sciences, Žitkova 22, 61662 Brno, Czech Republic
- ⁷ Karlsruhe Nano Micro Facility (KNMFi), Karlsruhe Institute of Technology (KIT), Hermann-von-Helmholtz-Platz 1, 76344 Eggenstein-Leopoldshafen, Germany